2026 IEEE International Conference on Robotics and Automation (ICRA 2026)
June 1-5, 2026. Vienna, Austria

A Passivity-Based Framework for Dynamic Arbitration between Trajectory and Force Tracking using Human Demonstration

Yeoil Yun, Youngwuk Kim, Junchul Gwak, Hyungpil Moon, Hyouk Ryeol Choi, and Ja Choon Koo

Abstract— **Learning from Demonstration (LfD) for contact-rich tasks faces a fundamental challenge: arbitrating between tracking a demonstrated trajectory and reproducing an interaction force. This paper introduces a novel one-shot LfD framework that resolves this conflict by leveraging the operator's grip force as an intuitive, continuous signal for arbitration. This signal allows the controller to seamlessly transition between a trajectory-tracking impedance controller and a force-tracking admittance controller, prioritizing path accuracy when the demonstrated grip was light and interaction force fidelity when it was firm. To ensure verifiably safe interaction, the adaptive control law is integrated within a dual-layer passivity assurance framework. This mechanism intelligently distributes potentially non-passive energy between an energy tank and adaptive null-space dissipation to guarantee energetic stability. The proposed framework was experimentally validated on a 7-DOF manipulator, demonstrating that the controller autonomously reproduces interaction forces and shows significant robustness against environmental position uncertainties, a scenario where conventional impedance controllers can fail.**

I. Introduction

The seamless integration of robots into human-centric environments for complex, contact-rich tasks such as assembly, polishing, and physical assistance remains a significant challenge in modern robotics [1], [2]. Learning from Demonstration (LfD) has emerged as a powerful and intuitive paradigm to transfer these sophisticated skills from a human user to a robot, bypassing the need for complex, model-based programming [3], [4]. However, for tasks involving physical contact, simply replicating a demonstrated trajectory is insufficient and often leads to failure. The robot must not only learn the geometric path but also understand and reproduce the nuanced interaction forces that are critical to task success [5], [6]. This has motivated significant research into learning variable impedance behaviors and force profiles to make robots more adaptive and compliant [7], [8], [9].

A fundamental dilemma in reproducing contact-rich tasks lies in the arbitration between trajectory tracking and force tracking. A controller that rigidly adheres to a learned trajectory will generate excessive forces and fail if the environment's geometry deviates even slightly from the demonstration conditions [10]. Conversely, a controller focused solely on replicating a force profile may drift from the intended path or become unstable if contact is lost or altered [11]. This necessitates a mechanism to dynamically decide which modality—position or force—to prioritize at any given moment. Prevailing approaches often rely on probabilistic models to blend policies or employ discrete, state-based switching to transition between different control modes [12], [13], [14], [15]. Other lines of research have attempted to infer operator intent more directly using physiological signals, such as electromyography (EMG), to estimate muscle co-contraction [16], [17]. However, such methods often face significant practical hurdles. EMG signals are notoriously noisy and require extensive filtering and subject-specific calibration. Furthermore, the need to attach electrodes to the operator's body can be cumbersome and restrictive, limiting the practicality of the approach in many settings.

In contrast, utilizing the operator's physical action, specifically the grip force, offers a more robust and scalable alternative. Unlike physiological signals, grip force is a mechanical signal with a high signal-to-noise ratio, ensuring low latency and immediate responsiveness without the need for extensive filtering. It also provides universality and simplicity; it eliminates the need for intrusive sensors or extensive subject-specific calibration, as modulating grip strength is an intrinsic human motor response to physical interaction. While the natural correlation between human grip force and interaction force can be complex and task-dependent, grip strength can be leveraged as an explicit communication channel for intent within a well-defined LfD framework. This leverages the natural human tendency to grip an object firmly when applying precise force. Within the proposed LfD framework, this intuitive action is transformed into an intentional signal for control arbitration—a firm grip signifies a phase of forceful interaction, while a lighter grip indicates free-space motion. This transforms the grip from a simple grasping action into a deliberate signal that encodes the desired arbitration strategy. However, creating a controller that is highly responsive to both human intent and external forces introduces significant safety challenges. As the controller's gains and desired objectives change dynamically, the system can become energetically active, posing a risk of instability. Ensuring the safety of both the human and the robot is paramount, and the concept of passivity provides a rigorous framework for guaranteeing stable physical interaction [18], [19].

Passivity-Based Control (PBC) has become a cornerstone for designing verifiably safe interaction controllers. By ensuring that the robot cannot generate more energy than what has been injected into it, passivity prevents the system from

*This work was supported by the Technology Innovation Program (2410002650, Development of a mobile manipulator robot system based on multi-collaboration for manipulating and assembling 500 kg large and heavy parts) funded by the Ministry of Trade Industry & Energy (MOTIE, Korea).

The authors are with School of Mechanical Engineering, Sungkyunkwan University, Suwon, Korea. Corresponding author: Ja Choon Koo jckoo@skku.edu

exhibiting unstable, runaway behaviors. A particularly effective tool in modern PBC is the energy tank, which allows the system to temporarily violate passivity for short-term performance gains while keeping the overall energy budget bounded and safe [20], [21], [22]. For redundant manipulators, this energy management can be seamlessly integrated within a hierarchical control framework. This architecture allows safety-related objectives, such as energy dissipation, to be allocated to the robot's null space, ensuring that they do not interfere with the primary task being executed by the end-effector [23], [24]. This principle of decoupling tasks and managing energy at a system level forms a robust foundation for building advanced, high-performance LfD frameworks.

This paper builds upon these principles to propose a novel LfD framework that ensures passivity while dynamically arbitrating between trajectory and force tracking using human demonstration. The main contributions are:

- A novel LfD framework that leverages operator grip force as a continuous, intuitive, and intentional signal to dynamically and smoothly arbitrate between trajectory tracking and force interaction controllers.
- The design of a reproduction controller that robustly replicates demonstrated force profiles, even in the presence of significant positional uncertainties in the environment.
- The seamless integration of this adaptive LfD controller with a sophisticated dual-layer passivity assurance mechanism, which features a novel dynamic arbitration function to intelligently manage energy between an energy tank and null-space dissipation.
- Experimental validation of the entire framework on a 7-degree-of-freedom (7-DOF) manipulator performing a contact-rich tracing task, demonstrating superior and safer performance compared to a conventional impedance controller baseline.

The remainder of this paper is organized as follows. Section II details the proposed control framework, including the hierarchical controller design, the LfD stages, and the dual-layer passivity analysis. Section III presents the experimental setup, procedures, and a discussion of the results. Finally, Section IV concludes the paper and suggests directions for future work.

II. Proposed Control Framework

A. Fundamental Principle: Hierarchical Dynamic Control

This study employs the hierarchical control framework proposed in [23] to decouple and manage the task-space and null-space dynamics of a redundant manipulator with $n > 6$ DOF. The governing dynamic equation of the manipulator is given by:

$$\boldsymbol{M}(\boldsymbol{q})\ddot{\boldsymbol{q}} + \boldsymbol{C}(\boldsymbol{q},\dot{\boldsymbol{q}})\dot{\boldsymbol{q}} + \boldsymbol{g}(\boldsymbol{q}) = \boldsymbol{\tau} + \boldsymbol{\tau}_{\text{ext}} \tag{1}$$

where $\boldsymbol{q} \in \mathbb{R}^n$ represents the vector of joint angles, $\boldsymbol{M}(\boldsymbol{q})$ is the inertia matrix, $\boldsymbol{C}(\boldsymbol{q},\dot{\boldsymbol{q}})$ is the matrix of Coriolis and centrifugal terms, $\boldsymbol{g}(\boldsymbol{q})$ is the gravitational torque, and $\boldsymbol{\tau}$ is the applied control torque. The external torque, $\boldsymbol{\tau}_{\text{ext}}$, is defined based on the operational phase. During the *demonstration phase*, it comprises both human-applied torque $\boldsymbol{\tau}_h$ and environmental interaction torque $\boldsymbol{\tau}_e$ (i.e., $\boldsymbol{\tau}_{\text{ext}} = \boldsymbol{\tau}_h + \boldsymbol{\tau}_e$). Conversely, during the autonomous *reproduction phase*, it is assumed to consist solely of the environmental interaction torque (i.e., $\boldsymbol{\tau}_{\text{ext}} = \boldsymbol{\tau}_e$).

To define the end-effector's task-space velocity $\dot{\boldsymbol{x}} \in \mathbb{R}^6$ and the kinematically decoupled null-space velocity $\dot{\boldsymbol{x}}_n \in \mathbb{R}^{n-6}$, an extended Jacobian matrix $\boldsymbol{J}_e(\boldsymbol{q}) \in \mathbb{R}^{n\times n}$ is utilized.

$$\dot{\boldsymbol{x}}_e = \begin{bmatrix} \dot{\boldsymbol{x}} \\ \dot{\boldsymbol{x}}_n \end{bmatrix} = \begin{bmatrix} \boldsymbol{J}(\boldsymbol{q}) \\ \boldsymbol{N}(\boldsymbol{q}) \end{bmatrix} \dot{\boldsymbol{q}} = \boldsymbol{J}_e(\boldsymbol{q})\dot{\boldsymbol{q}} \tag{2}$$

In this formulation, $\boldsymbol{J}(\boldsymbol{q})$ is the end-effector Jacobian. The null-space Jacobian, $\boldsymbol{N}(\boldsymbol{q}) = (\boldsymbol{Z}\boldsymbol{M}\boldsymbol{Z}^T)^{-1}\boldsymbol{Z}\boldsymbol{M}$, is constructed to ensure that $\boldsymbol{J}_e$ remains non-singular. Here, $\boldsymbol{Z}$ constitutes a basis for the null space of $\boldsymbol{J}^T$. This allows the robot's dynamics in (1) to be reformulated in the extended task space as:

$$\boldsymbol{\Lambda}_e\ddot{\boldsymbol{x}}_e + \boldsymbol{\mu}_e\dot{\boldsymbol{x}}_e = \boldsymbol{J}_e^{-T}\big(-\boldsymbol{g}(\boldsymbol{q}) + \boldsymbol{\tau} + \boldsymbol{\tau}_{\text{ext}}\big) \tag{3}$$

where $\boldsymbol{\Lambda}_e = \boldsymbol{J}_e^{-T}\boldsymbol{M}\boldsymbol{J}_e^{-1}$ is the inertia matrix in the extended task space, and $\boldsymbol{\mu}_e$ is the Coriolis matrix:

$$\boldsymbol{\mu}_e = \boldsymbol{\Lambda}_e\left(\boldsymbol{J}_e\boldsymbol{M}^{-1}\boldsymbol{C} - \dot{\boldsymbol{J}}_e\right)\boldsymbol{J}_e^{-1} = \begin{bmatrix} \boldsymbol{\mu}_x & \boldsymbol{\mu}_{xn} \\ \boldsymbol{\mu}_{nx} & \boldsymbol{\mu}_n \end{bmatrix}. \tag{4}$$

The off-diagonal terms of $\boldsymbol{\mu}_e$, namely $\boldsymbol{\mu}_{xn}$ and $\boldsymbol{\mu}_{nx}$, introduce dynamic coupling between the primary and secondary tasks. To counteract this interference, the following decoupling torque is applied:

$$\boldsymbol{\tau}_\mu = \boldsymbol{J}_e^T\begin{bmatrix} 0 & \boldsymbol{\mu}_{xn} \\ \boldsymbol{\mu}_{nx} & 0 \end{bmatrix}\boldsymbol{J}_e\dot{\boldsymbol{q}}. \tag{5}$$

It should be noted that this decoupling action is passive, as the input power $\dot{\boldsymbol{q}}^T\boldsymbol{\tau}_\mu = 0$ due to the skew-symmetric property of the central matrix in the expression. Consequently, the total control torque $\boldsymbol{\tau}$ applied to the robot is a summation of four components: the task-space wrench $\boldsymbol{F}_a$, the null-space wrench $\boldsymbol{F}_n$, the gravity compensation, and the decoupling torque:

$$\boldsymbol{\tau} = \boldsymbol{g}(\boldsymbol{q}) + \boldsymbol{J}^T\boldsymbol{F}_a + \boldsymbol{N}^T\boldsymbol{F}_n + \boldsymbol{\tau}_\mu. \tag{6}$$

This control architecture serves as the foundation for implementing the different stages of the LfD framework. For both the demonstration and reproduction phases, a consistent control law is applied to the null space to regulate the manipulator's posture. This is achieved using an adaptive joint angle PD controller, and the control input for the null-space wrench, $\boldsymbol{F}_n$, is formulated as:

$$\boldsymbol{F}_n = \boldsymbol{K}_{n,p}\gamma_n\tilde{\boldsymbol{q}} + \boldsymbol{K}_{n,d}\frac{d}{dt}(\gamma_n\tilde{\boldsymbol{q}}). \tag{7}$$

Here, the joint error $\tilde{\boldsymbol{q}}$ is defined as $\tilde{\boldsymbol{q}} = \boldsymbol{q}_d - \boldsymbol{q}$, with $\boldsymbol{q}_d$ being a desired home posture. The term $\gamma_n(t)$ is a time-varying adaptive gain, and the constant matrices $\boldsymbol{K}_{n,p}$ and $\boldsymbol{K}_{n,d}$ are the positive-definite proportional and derivative gains, respectively. The formulation of this controller ensures that the derivative term accounts for changes in both the

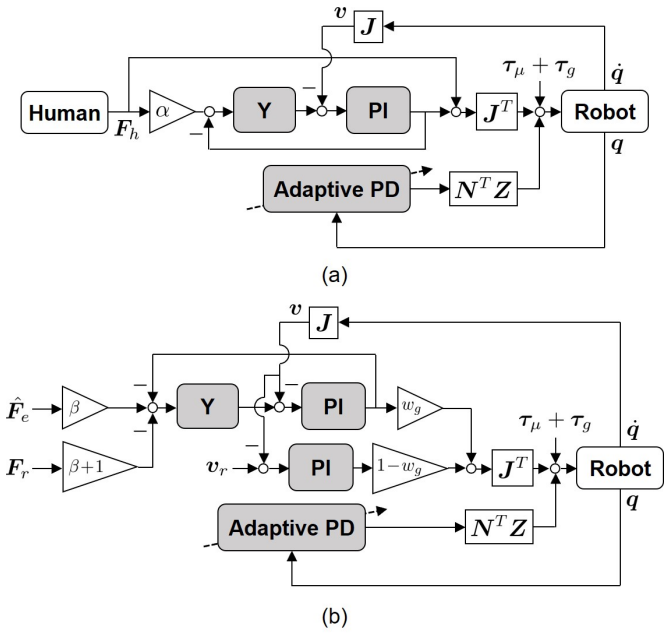

Fig. 1. Block diagram of the proposed control architecture. (a) In the demonstration stage, an admittance controller responds to human input $\boldsymbol{F}_h$. (b) In the reproduction stage, the outputs of the admittance-based interaction controller and the PI-based trajectory controller are blended using the grip-based weight w_g.

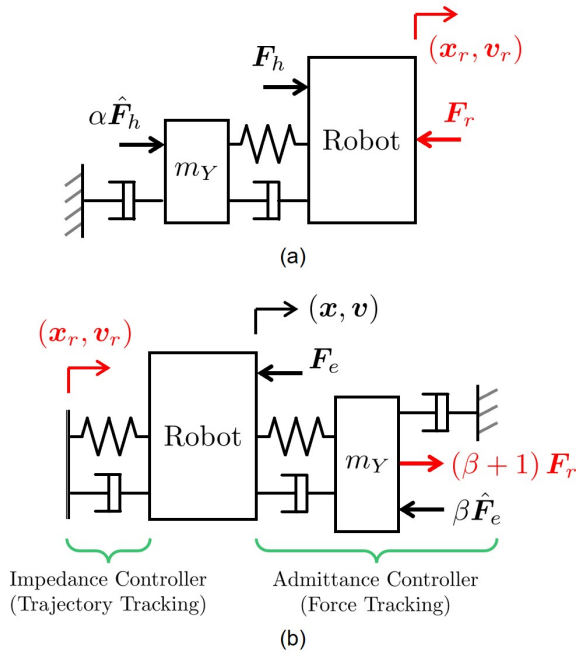

Fig. 2. Conceptual models of the control strategies. (a) During the demonstration phase, an admittance controller creates a compliant response to the human force $\boldsymbol{F}_h$. (b) During the reproduction phase, the system arbitrates between an impedance controller for trajectory tracking and an admittance controller for replicating the interaction wrench.

tracking error and the adaptive gain. The subsequent section will elaborate on how the task-space wrench $\boldsymbol{F}_a$ and this adaptive null-space controller are specifically designed for the human demonstration and task reproduction phases.

B. Learning and Reproduction Framework

The overall architecture of the proposed control framework is illustrated in the block diagram in Fig. 1. The framework consists of three distinct stages, with the detailed mechanism for each stage described below.

1) Stage 1: Recording Human Demonstration Data: During the demonstration stage, the robot is designed to compliantly follow the wrench $\boldsymbol{F}_h$ applied by a human operator. This behavior is achieved through the combination of an admittance model and an inner-loop tracking controller, as depicted by the equivalent mass-spring-damper system in Fig. 2(a). The control inputs are governed by:

$$\boldsymbol{F}_a^* = \boldsymbol{K}_i^* \tilde{\boldsymbol{x}}^* + \boldsymbol{K}_p^* \dot{\tilde{\boldsymbol{x}}}^* \tag{8}$$

$$\bar{\boldsymbol{\Lambda}}^* \ddot{\boldsymbol{x}}_d^* + \bar{\boldsymbol{\mu}}^* \dot{\boldsymbol{x}}_d^* = \alpha \hat{\boldsymbol{F}}_h^* - \boldsymbol{F}_a^* \tag{9}$$

where the tracking error is $\tilde{\boldsymbol{x}}^* = \boldsymbol{x}_d^* - \boldsymbol{x}^*$. The terms $\bar{\boldsymbol{\Lambda}}^*$ and $\bar{\boldsymbol{\mu}}^*$ represent the virtual inertia and damping matrices designed for compliant human interaction. The coefficient α is a gain that adjusts the static equilibrium of the external interaction wrench. Here, the hat notation $(\hat{\cdot})$ denotes a value obtained through real-time measurement or estimation. The superscript $(\cdot)^*$ is used to denote all states and parameters associated with the demonstration phase. With the negative feedback of $\boldsymbol{F}_a^*$ in (9), the admittance model behaves as if it is connected to the robot's actual end-effector position through a virtual spring-damper system.

According to this formulation, when the system reaches a static equilibrium ($\ddot{\boldsymbol{x}}_d^* = \dot{\boldsymbol{x}}_d^* = \boldsymbol{0}$), the total driving wrench $\boldsymbol{F}_r$ acts on the virtual admittance. This wrench consists of the active assistance term based on the measured force ($\alpha\hat{\boldsymbol{F}}_h^*$) and the actual physical human wrench ($\boldsymbol{F}_h^*$), formulated as $\boldsymbol{F}_r = \alpha\hat{\boldsymbol{F}}_h^* + \boldsymbol{F}_h^*$. This effectively amplifies the human's applied wrench by a tunable factor, making the controller suitable for applications such as force augmentation. Throughout this process, several data streams are recorded: the end-effector trajectory $\boldsymbol{x}_r(t) = \boldsymbol{x}^*(t)$, velocity $\dot{\boldsymbol{x}}_r(t) = \dot{\boldsymbol{x}}^*(t)$, the measured grip force $g(t) \geq 0$, and the estimated external contact wrench $\boldsymbol{F}_r(t)$.

2) Stage 2: Grip Force Processing and Weight Generation: The operator's grip force during the demonstration is a crucial piece of information, as it implicitly contains the intent to interact with the environment. The raw grip force data, $g(t)$, is post-processed into an interaction weight $w_g(t) \in [0, 1]$. This is achieved by normalizing and saturating the signal with respect to a threshold g_{sat}, which was determined empirically based on the operator's comfortable maximum grip force during preliminary trials:

$$w_g(t) = \min\left(\frac{\max(0, g(t))}{g_{\text{sat}}}, 1\right). \tag{10}$$

This weight is then used during the reproduction stage to dynamically arbitrate between trajectory tracking and interaction modes.

3) Stage 3: Weight-Based Task Reproduction: In the task reproduction stage, a hybrid impedance/admittance control strategy is employed to simultaneously track the demonstrated trajectory and replicate the recorded interaction. The primary task wrench $\boldsymbol{F}_a$ is determined by blending the outputs of a trajectory tracking impedance controller and an interaction controller in real-time, using the weight $w_g(t)$.

The trajectory tracking impedance controller generates an impedance wrench $\boldsymbol{F}_z$ to minimize the error $\tilde{\boldsymbol{x}} = \boldsymbol{x}_r - \boldsymbol{x}$ between the demonstrated trajectory $\boldsymbol{x}_r(t)$ and the current robot trajectory $\boldsymbol{x}(t)$:

$$\boldsymbol{F}_z = \boldsymbol{K}_{i,z}\tilde{\boldsymbol{x}} + \boldsymbol{K}_{p,z}\dot{\tilde{\boldsymbol{x}}}. \tag{11}$$

The interaction controller, depicted in Fig. 2(b), generates an admittance-based wrench $\boldsymbol{F}_y$ to facilitate compliant interaction. It takes the recorded external wrench $\boldsymbol{F}_r(t)$ and the currently measured external wrench $\hat{\boldsymbol{F}}_e(t)$ as inputs. The trajectory error for this controller is defined as $\tilde{\boldsymbol{x}}_y = \boldsymbol{x}_y - \boldsymbol{x}$, and its dynamics are:

$$\bar{\boldsymbol{\Lambda}}\ddot{\boldsymbol{x}}_y + \bar{\boldsymbol{\mu}}\dot{\boldsymbol{x}}_y = \beta\hat{\boldsymbol{F}}_e - (\beta+1)\boldsymbol{F}_r - \boldsymbol{F}_y \tag{12}$$

$$\boldsymbol{F}_y = \boldsymbol{K}_{i,y}\tilde{\boldsymbol{x}}_y + \boldsymbol{K}_{p,y}\dot{\tilde{\boldsymbol{x}}}_y. \tag{13}$$

When this subsystem reaches static equilibrium ($\ddot{\boldsymbol{x}}_y = \dot{\boldsymbol{x}}_y = \boldsymbol{0}$), the commanded interaction wrench becomes $\boldsymbol{F}_e = (\beta+1)\boldsymbol{F}_r - \beta\hat{\boldsymbol{F}}_e$. This relationship ensures that if the actual interaction wrench approximates the desired one ($\boldsymbol{F}_e \approx \hat{\boldsymbol{F}}_e$), then the system drives the actual wrench to match the recorded one ($\hat{\boldsymbol{F}}_e \approx \boldsymbol{F}_r$). The parameter β acts as a sensitivity gain on the error between the recorded and measured wrenches; a larger β results in a more aggressive correction.

The outputs of these two controllers are integrated to form the final task-space wrench $\boldsymbol{F}_a$ from (6), defined as their weighted sum:

$$\boldsymbol{F}_a = (1 - w_g(t))\boldsymbol{F}_z + w_g(t)\boldsymbol{F}_y. \tag{14}$$

This control law enables the robot to seamlessly arbitrate its behavior: in non-contact phases where the operator's grip was light ($w_g \approx 0$), it precisely tracks the demonstrated trajectory. In contact-rich phases where the grip was firm ($w_g \approx 1$), it compliantly responds to external forces, thereby effectively reproducing the intended interaction.

C. Energy Monitoring and Dual-Layer Passivity Assurance

The input gains α and β, introduced to enhance performance, can inject energy into the system by increasing its sensitivity to external wrenches. This poses a potential risk to the system's passivity, which could lead to instability. Therefore, to guarantee safe human-robot interaction and stable contact-rich task execution, a dual-layer safety mechanism inspired by [25] is employed to manage the system's energy and ensure overall passivity.

For the passivity analysis, the total stored energy of the system, S, is defined as the sum of its kinetic and potential energies. During the reproduction phase, this is given by:

$$\begin{aligned} S = &\underbrace{\frac{1}{2}\dot{\boldsymbol{q}}^T\boldsymbol{M}\dot{\boldsymbol{q}}}_{T_{\text{robot}}} + \underbrace{\frac{1}{2}\dot{\boldsymbol{x}}_y^T\bar{\boldsymbol{\Lambda}}\dot{\boldsymbol{x}}_y}_{T_{\text{adm}}} + \underbrace{\frac{1}{2}\tilde{\boldsymbol{x}}^T\boldsymbol{K}_{i,z}\tilde{\boldsymbol{x}}}_{V_{\text{imp}}} \\ &+ \underbrace{\frac{1}{2}\tilde{\boldsymbol{x}}_y^T\boldsymbol{K}_{i,y}\tilde{\boldsymbol{x}}_y}_{V_{\text{int}}} + \underbrace{\frac{1}{2}\gamma_n^2\tilde{\boldsymbol{q}}^T\boldsymbol{K}_{n,p}\tilde{\boldsymbol{q}}}_{V_{\text{null}}} + E_t. \end{aligned} \tag{15}$$

Here, V_{imp} and V_{int} are the potential energies stored by the stiffness gains $\boldsymbol{K}_{i,z}$ and $\boldsymbol{K}_{i,y}$, which act as virtual springs for the trajectory tracking and interaction controllers, respectively.

According to the law of conservation of energy, the rate of change of the total stored energy, $\dot{S}$, must equal the sum of the power flows. The time derivative of S can be expressed as:

$$\dot{S} = \dot{W}_{\text{ext}} + P_{\text{ID}} - P_{\text{PD}} + \dot{V}_{\text{null}} + \dot{E}_t \tag{16}$$

where $\dot{W}_{\text{ext}} = \dot{\boldsymbol{q}}^T\boldsymbol{\tau}_{\text{ext}}$ is the power injected by the external environment. The term P_{ID} represents the power generated internally by the controller, which is indefinite in sign and thus potentially non-passive. The term P_{PD} is the power dissipated by damping elements, which is always non-negative ($P_{\text{PD}} \geq 0$). These power terms are defined as:

$$\begin{aligned} P_{\text{ID}} &= \dot{\boldsymbol{x}}^T\boldsymbol{F}_a + \dot{\boldsymbol{x}}_n^T\boldsymbol{F}_n \\ &\quad + \dot{\boldsymbol{x}}_y^T(\beta\hat{\boldsymbol{F}}_e - (\beta+1)\boldsymbol{F}_r - \boldsymbol{F}_y) \\ &\quad + \dot{\tilde{\boldsymbol{x}}}^T\boldsymbol{F}_z + \dot{\tilde{\boldsymbol{x}}}_y^T\boldsymbol{F}_y \\ &= \dot{\boldsymbol{x}}^T\left((w_g(t)-1)\,\boldsymbol{F}_y - w_g(t)\boldsymbol{F}_z\right) + \dot{\boldsymbol{x}}_n^T\boldsymbol{F}_n \\ &\quad + \dot{\boldsymbol{x}}_y^T(\beta\hat{\boldsymbol{F}}_e - (\beta+1)\boldsymbol{F}_r) + \dot{\boldsymbol{x}}_r^T\boldsymbol{F}_z \end{aligned} \tag{17a}$$

$$P_{\text{PD}} = \dot{\boldsymbol{x}}_y^T\bar{\boldsymbol{\mu}}\dot{\boldsymbol{x}}_y + \dot{\tilde{\boldsymbol{x}}}^T\boldsymbol{K}_{p,z}\dot{\tilde{\boldsymbol{x}}} + \dot{\tilde{\boldsymbol{x}}}_y^T\boldsymbol{K}_{p,y}\dot{\tilde{\boldsymbol{x}}}_y. \tag{17b}$$

It is important to note that the proportional gains of the task-space controllers, $\boldsymbol{K}_{p,z}$ and $\boldsymbol{K}_{p,y}$, act as dampers on the velocity error and are therefore included in the dissipative power term P_{PD}.

To systematically manage the energy injection from P_{ID}, the dual-layer safety mechanism is utilized. Instead of relying solely on the tank level, this work introduces a dynamic arbitration function, $\psi(E_t, P_{\text{ID}}, P_{\text{PD}})$, which considers both the current energy level in the tank (E_t) and the severity of the net power injection ($P_{\text{ID}} - P_{\text{PD}}$). This allows the system to smoothly transition between performance-oriented and safety-oriented behaviors. The arbitration is governed by a continuous, dynamic function ψ designed to act as a smooth, risk-aware switch. The function's input z combines the system's current energy state (E_t) with the severity of power injection ($P_{\text{ID}} - P_{\text{PD}}$). This ensures that the system reacts gently to minor non-passive behaviors but aggressively shifts towards dissipation when facing significant energy injection, especially when the energy tank is nearly full. This policy is implemented as:

$$\begin{aligned} \psi(E_t, P_{\text{ID}}, P_{\text{PD}}) &= \frac{1}{2}\left(\frac{z}{\sqrt{z^2+1}} + 1\right) \\ \text{where } z &= \left(\frac{E_t}{E_{t,\max}} - 0.5\right)(P_{\text{ID}} - P_{\text{PD}}). \end{aligned} \tag{18}$$

This arbitration law provides an effective risk management strategy, tolerating minor non-passive behaviors to maintain performance while responding strictly to significant energy injections to ensure stability.

1) First Safety Layer: Energy Tank (E_t): The energy tank serves as a buffer, absorbing a portion of the potentially non-passive power, governed by:

$$\dot{E}_t = -\psi \left(P_{\text{ID}} - P_{\text{PD}} \right). \tag{19}$$

Additionally, a safety switch can be applied to the final wrench output, deactivating the controllers ($\boldsymbol{F}_a = \boldsymbol{F}_n = \boldsymbol{0}$) if the tank's energy is depleted ($E_t \leq 0$).

2) Second Safety Layer: Adaptive Null-Space Control: The second layer is responsible for dissipating the remaining portion of the net injected power, $(1-\psi)\left(P_{\text{ID}} - P_{\text{PD}}\right)$, by redirecting it to the null space. This leverages the technique proposed in [25], where the adaptive gain γ_n is modulated such that the rate of change of the null-space potential energy exactly cancels the bypassed power. The gain is calculated as:

$$\gamma_n = \sqrt{\frac{\lambda_2}{\lambda_1}}, \tag{20}$$

where

$$\lambda_1 = \frac{1}{2} \tilde{\boldsymbol{q}}^T \boldsymbol{K}_{n,p} \tilde{\boldsymbol{q}} \tag{21a}$$

$$\lambda_2 = \int_0^t \left((\psi - 1) \left(P_{\text{ID}} - P_{\text{PD}} \right) - \varepsilon \right) \, dt + \lambda_1 |_{t=0}. \tag{21b}$$

The parameter $\varepsilon \geq 0$ is a tunable energy dissipation rate, which allows a designer to enforce a desired level of strict passivity. This calculation of the adaptive gain results in:

$$\dot{V}_{\text{null}} = (\psi - 1) \left(P_{\text{ID}} - P_{\text{PD}} \right) - \varepsilon. \tag{22}$$

The design objective of the dual-layer safety mechanism is to ensure that $\dot{V}_{\text{null}} + \dot{E}_t = -(P_{\text{ID}} - P_{\text{PD}}) - \varepsilon$, thereby canceling the non-passive term. Substituting this relationship into the energy conservation equation (16) yields the following passivity inequality:

$$\dot{S} - \dot{W}_{\text{ext}} = -\varepsilon \leq 0. \tag{23}$$

This inequality signifies that the energy stored in the system cannot exceed the work done on it by the external environment, plus any initial energy. Thus, all non-passive energy generated by the controller is systematically neutralized, guaranteeing the passivity of the entire system.

3) Application to the Demonstration Stage: The same passivity framework can be applied to the demonstration stage. The total stored energy during demonstration, S^*, is defined as:

$$\begin{aligned} S^* = & \underbrace{\frac{1}{2} \dot{\boldsymbol{q}}^{*T} \boldsymbol{M} \dot{\boldsymbol{q}}^*}_{T^*_{\text{robot}}} + \underbrace{\frac{1}{2} \dot{\boldsymbol{x}}_d^{*T} \bar{\boldsymbol{\Lambda}}^* \dot{\boldsymbol{x}}_d^*}_{T^*_{\text{adm}}} + \underbrace{\frac{1}{2} \tilde{\boldsymbol{x}}_d^{*T} \boldsymbol{K}_i^* \tilde{\boldsymbol{x}}_d^*}_{V^*_{\text{track}}} \\ & + \underbrace{\frac{1}{2} \gamma_n^{*2} \tilde{\boldsymbol{q}}^{*T} \boldsymbol{K}_{n,p} \tilde{\boldsymbol{q}}^*}_{V^*_{\text{null}}} + E_t. \end{aligned} \tag{24}$$

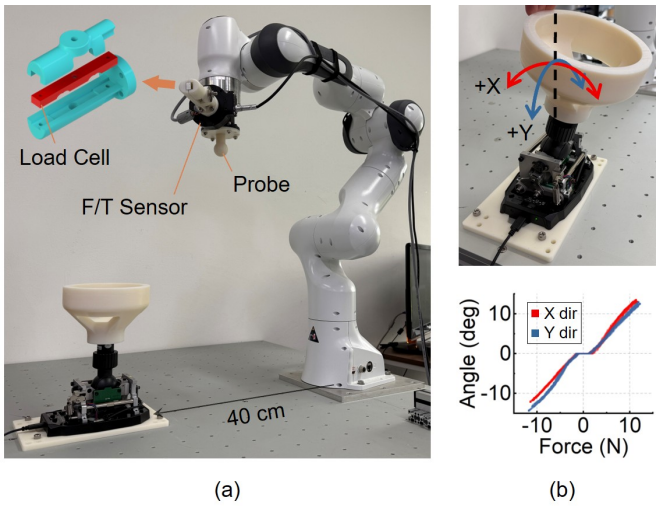

(a) (b)

Fig. 3. The experimental setup. (a) A 7-DOF Franka Emika Panda manipulator equipped with a custom end-effector, including an F/T sensor, a grip-force handle with an integrated load cell, and an interaction probe. (b) The interaction environment, a 2-DOF compliant joystick, and its force-angle characteristic, which is used as the performance metric.

The corresponding indefinite and dissipative power terms, P^*_{ID} and P^*_{PD}, are:

$$\begin{aligned} P^*_{\text{ID}} &= \dot{\boldsymbol{x}}^{*T} \boldsymbol{F}_a^* + \dot{\boldsymbol{x}}_n^{*T} \boldsymbol{F}_n^* \\ &\quad + \dot{\boldsymbol{x}}_d^{*T} (\alpha \hat{\boldsymbol{F}}_h^* - \boldsymbol{F}_a^*) + \dot{\tilde{\boldsymbol{x}}}^{*T} \boldsymbol{F}_a^* \\ &= \dot{\boldsymbol{x}}_n^{*T} \boldsymbol{F}_n^* + \alpha \dot{\boldsymbol{x}}_d^{*T} \hat{\boldsymbol{F}}_h^* \end{aligned} \tag{25a}$$

$$P^*_{\text{PD}} = \dot{\boldsymbol{x}}_d^{*T} \bar{\boldsymbol{\mu}}^* \dot{\boldsymbol{x}}_d^* + \dot{\tilde{\boldsymbol{x}}}^{*T} \boldsymbol{K}_p^* \dot{\tilde{\boldsymbol{x}}}^*. \tag{25b}$$

The net power injection $P^*_{\text{ID}} - P^*_{\text{PD}}$ can be canceled using the same dual-layer safety mechanism, thus guaranteeing stable interaction during the demonstration phase.

III. Experiments

A. Experimental Setup

To validate the performance of the proposed LfD framework, an experimental setup was configured as shown in Fig. 3(a). A 7-DOF redundant manipulator (Franka Emika Panda) was used. Its end-effector was equipped with a 6-axis F/T sensor (AIDIN Robotics AFT200), a custom handle instrumented with a load cell to measure the operator's grip force, and a spherical probe for physical interaction. The physical separation of the grip-sensing handle and the interaction probe is a deliberate design choice. It prevents the operator's grasping actions from introducing direct disturbances at the contact point, allowing for the distinct recording of interaction data and user intent.

The interaction environment consists of a 2-DOF compliant joystick (Thrustmaster AVA Base), as shown in Fig. 3(b). The device exhibits a mechanical impedance where the restoring force is proportional to its tilt angle. Consequently, the joystick's tilt angle serves as the primary performance metric, representing the interaction force between the probe and the environment. The human teaching wrench ($\hat{\boldsymbol{F}}_h$) was measured by the F/T sensor. To distinguish interaction

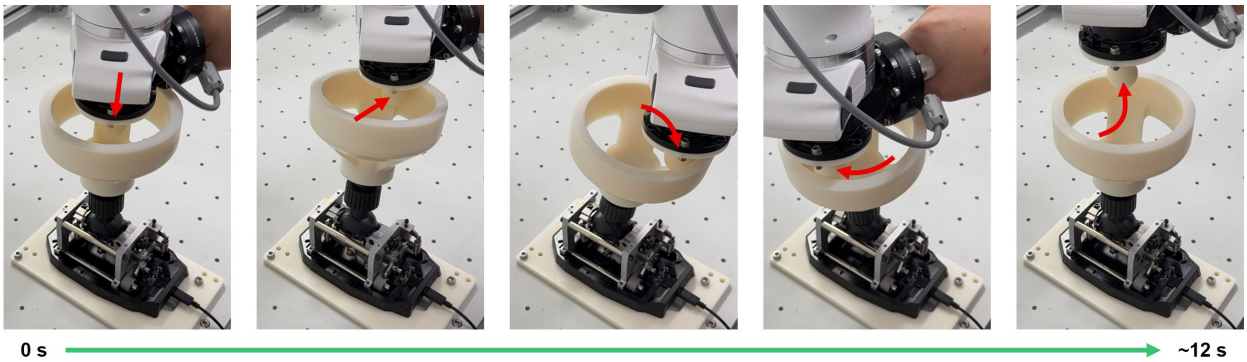

Fig. 4. Image sequence of the human demonstration phase. The operator guides the robot's probe to trace the inner wall of the wheel structure. The entire interaction lasts for approximately 12 seconds.

TABLE I
CONTROLLER PARAMETERS

Parameter	Value	Unit
Demonstration Phase		
$\bar{\boldsymbol{\Lambda}}^*$	$1 \cdot \boldsymbol{I}_6$	kg, kg·m^2
$\bar{\boldsymbol{\mu}}^*$	$5 \cdot \boldsymbol{I}_6$	Ns/m, Nms/rad
$\boldsymbol{K}_i^*$	$200 \cdot \boldsymbol{I}_6$	N/m, Nm/rad
$\boldsymbol{K}_p^*$	$10 \cdot \boldsymbol{I}_6$	Ns/m, Nms/rad
α	1	-
Reproduction Phase		
$\boldsymbol{K}_{i,z}$	$\mathrm{diag}(800, 800, 800, 50, 50, 50)$	N/m, Nm/rad
$\boldsymbol{K}_{p,z}$	$2\sqrt{\boldsymbol{K}_{i,z}}$	Ns/m, Nms/rad
$\boldsymbol{\Lambda}$	$\mathrm{diag}(0.1, 0.1, 0.1, 0.2, 0.2, 0.2)$	kg, kg·m^2
$\bar{\boldsymbol{\mu}}$	$\mathrm{diag}(0.5, 0.5, 0.5, 1, 1, 1)$	Ns/m, Nms/rad
$\boldsymbol{K}_{i,y}$	$600 \cdot \boldsymbol{I}_6$	N/m, Nm/rad
$\boldsymbol{K}_{p,y}$	$20 \cdot \boldsymbol{I}_6$	Ns/m, Nms/rad
β	1	-
Common Parameters		
$\boldsymbol{K}_{n,p}$	$2 \cdot \boldsymbol{I}_7$	Nm/rad
$\boldsymbol{K}_{n,d}$	$2 \cdot \boldsymbol{I}_7$	Nms/rad
$\boldsymbol{q}_d$	$[0, 0, 0, -0.5\pi, 0, 0.8\pi, 0]^T$	rad
g_{sat}	110	N
$E_{t,\text{init}}$	1.5	J
$E_{t,\text{max}}$	3	J
ε	0	J/s
k_{MOB}	30	-

wrenches from human-applied forces, the external contact wrench was estimated using a momentum observer [26] for both the recording of $\boldsymbol{F}_r(t)$ during demonstration and the real-time measurement of $\hat{\boldsymbol{F}}_e(t)$ during reproduction. The momentum observer has a first-order low-pass filter response,

$$\frac{\hat{\boldsymbol{F}}_e(s)}{\boldsymbol{F}_e(s)} = \frac{k_{\text{MOB}}}{s + k_{\text{MOB}}}, \tag{26}$$

which allows it to be integrated into the system without violating passivity [27].

The key controller parameters used in the experiments are listed in Table I. These parameters were selected empirically to ensure stable performance within the robot's bandwidth. Specifically, the integral gains ($\boldsymbol{K}_{i,z}, \boldsymbol{K}_{i,y}$) were tuned to balance compliance and tracking accuracy, while the damping gains ($\boldsymbol{K}_{p,z}, \boldsymbol{K}_{p,y}$) were adjusted to yield a stable, well-damped response with minimal overshoot. The safety-related parameters, such as the maximum tank energy $E_{t,\text{max}}$ and the dissipation rate ε, were chosen conservatively to prioritize safety over performance aggressiveness. This empirical tuning proved robust, as the same set of parameters maintained stability across all tested conditions without requiring retuning.

B. Task and Procedure

The experimental task was a contact-based operation, requiring the robot's probe to trace the inner wall of a wheel-shaped structure mounted on the AVA Base. This task was specifically chosen as a canonical example of contact-rich manipulation, as the continuous constrained motion along a concave surface with varying curvature imposes stricter stability requirements than simple planar contact tasks. The experiment was conducted in two sequential stages.

First, as illustrated in Fig. 4, a human operator guided the robot by its handle, demonstrating the circular path along the wheel's inner surface. During this demonstration, which lasted approximately 12 seconds, the robot's trajectory, grip force, and interaction wrench were recorded.

Second, the robot autonomously reproduced the task based on the recorded data. The reproduction is executed entirely based on the recorded signals without any real-time human command. To evaluate the controller's robustness and adaptability against environmental uncertainty, the reproduction was performed under three different conditions: (1) nominal, at the same location as the demonstration; (2) with a -15 mm offset in the X-axis; and (3) with a +15 mm offset in the Y-axis. These offset conditions serve as a rigorous stress test for the proposed arbitration mechanism.

C. Results and Discussion

To provide a clear performance benchmark, a trajectory-only impedance controller was established as a baseline for comparison. This baseline is equivalent to setting the grip weight to zero ($w_g(t) = 0$) in (14) for the entire duration. Consequently, the robot exclusively tracks the recorded trajectory ($\boldsymbol{x}_r$) without any regard for the demonstrated interaction wrench.

Fig. 5 compares the interaction force tracking performance of the proposed controller and the baseline under the three

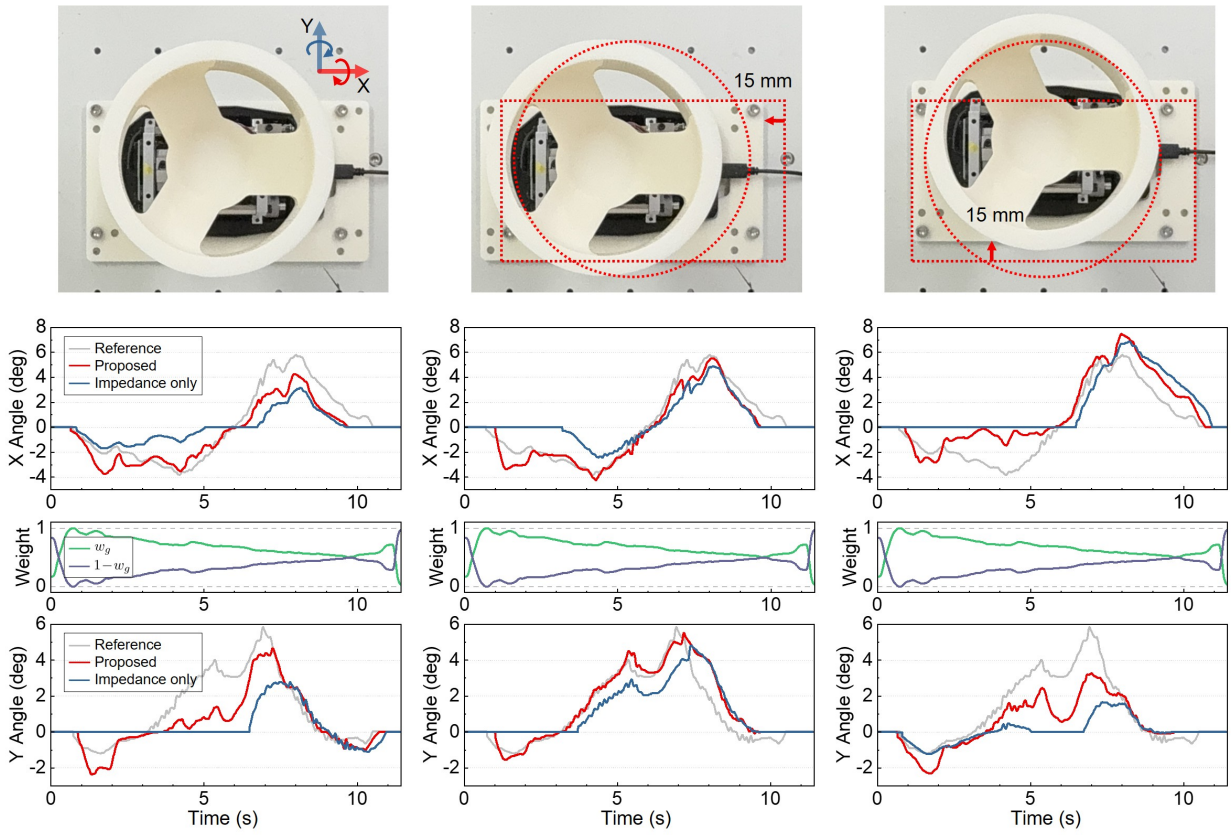

Fig. 5. Force tracking performance under three conditions: (left) nominal position, (middle) -15 mm offset in X, and (right) +15 mm offset in Y. The plots show the joystick tilt angle, representing the interaction force. The proposed controller (red) demonstrates superior force tracking compared to the trajectory-only impedance controller (blue), especially in the presence of positional uncertainty. The weight plot (w_g, green) shows the dynamic arbitration in action.

conditions. In the nominal case (left column), the proposed controller significantly reduced the tracking error (RMSE) compared to the baseline, from 1.77 deg to 1.04 deg in the X-axis and from 1.86 deg to 1.09 deg in the Y-axis.

The advantages of the proposed framework are most evident in the presence of positional disturbances (middle and right columns). The trajectory-only controller (blue) rigidly follows the demonstrated path and thus exhibits larger force deviations when the contact condition changes due to the imposed positional offsets. In contrast, the proposed controller leverages the recorded grip-based weight to prioritize interaction control during contact-rich phases. As shown by the weight plot, w_g remains high ($w_g \approx 1$) during the contact-rich phases, which increases the contribution of the admittance-based interaction controller ($\boldsymbol{F}_y$) in (14). This enables the robot to compliantly adapt to the shifted environment while still reproducing the demonstrated interaction trend. As a result, the RMSE was reduced from 1.36 deg to 0.66 deg in the X-axis and from 0.96 deg to 0.62 deg in the Y-axis for the -15 mm offset case. For the +15 mm offset in Y, the RMSE was reduced from 1.97 deg to 1.47 deg in the X-axis and from 1.72 deg to 1.08 deg in the Y-axis.

Beyond the improved tracking accuracy, the safe execution of these contact transitions is inherently supported by the dual-layer passivity assurance mechanism described in Sec. II-C, which provides an energetic stability guarantee under dynamic arbitration. Furthermore, from a practical deployment perspective, while grip strength naturally varies across individuals, the proposed framework addresses this variance through the normalization parameter g_{sat}. A simple calibration step—measuring the operator's maximum comfortable grip force prior to the task—is sufficient to adapt the system to different users, ensuring consistent arbitration behavior regardless of individual strength differences.

IV. Conclusions

This paper presented a novel one-shot Learning from Demonstration (LfD) framework for contact-rich tasks that dynamically arbitrates between trajectory and force tracking. By leveraging the human operator's grip force as an intuitive and intentional signal, the proposed controller seamlessly transitions between prioritizing path accuracy in free space and replicating interaction forces during contact. This arbitration was integrated with a rigorous dual-layer passivity-based safety mechanism, featuring a dynamic arbitration function to ensure energetic stability throughout both demonstration and reproduction phases.

Experimental validation on a 7-DOF manipulator demonstrated that the proposed controller successfully reproduces demonstrated interaction forces with high fidelity. More im-

portantly, it showed significant robustness to environmental uncertainties where a conventional trajectory-only impedance controller failed. The results validate the effectiveness of using intentional physical cues for data-efficient task arbitration and pave the way for more intuitive and robust robotic learning. Future work will extend the validation to a broader set of tasks, including comparisons with other hybrid or probabilistic arbitration frameworks, and investigate the online learning of the controller's interaction parameters to further enhance the system's adaptability.

REFERENCES

[1] M. Suomalainen, Y. Karayiannidis, and V. Kyrki, "A survey of robot manipulation in contact," *Robotics and Autonomous Systems*, vol. 156, p. 104224, 2022.

[2] Y. Li, A. Sena, Z. Wang, X. Xing, J. Babič, E. van Asseldonk, and E. Burdet, "A review on interaction control for contact robots through intent detection," *Progress in Biomedical Engineering*, vol. 4, no. 3, p. 032004, 2022.

[3] B. D. Argall, S. Chernova, M. Veloso, and B. Browning, "A survey of robot learning from demonstration," *Robotics and Autonomous Systems*, vol. 57, no. 5, pp. 469–483, 2009.

[4] J. Fu, H. Huang, Z. Jin, A. Liu, W.-A. Zhang, L. Yu, W. Si, and C. Yang, "A survey on learning an autonomous dynamic system for human–robot skills transfer from demonstration," *Robotics and Computer-Integrated Manufacturing*, vol. 97, p. 103092, 2026.

[5] H. Yin, A. Varava, and D. Kragic, "Modeling, learning, perception, and control methods for deformable object manipulation," *Science Robotics*, vol. 6, no. 54, p. eabd8803, 2021.

[6] W. Si, N. Wang, and C. Yang, "A review on manipulation skill acquisition through teleoperation-based learning from demonstration," *Cognitive Computation and Systems*, vol. 3, no. 1, pp. 1–16, 2021.

[7] X. Zhang, L. Sun, Z. Kuang, and M. Tomizuka, "Learning variable impedance control via inverse reinforcement learning for force-related tasks," *IEEE Robotics and Automation Letters*, vol. 6, no. 2, pp. 2225–2232, 2021.

[8] W. Liu, J. Wang, Y. Wang, W. Wang, and C. Lu, "Forcemimic: Force-centric imitation learning with force-motion capture system for contact-rich manipulation," in *2025 IEEE International Conference on Robotics and Automation (ICRA)*, 2025, pp. 1105–1112.

[9] Z. Lu, N. Wang, and C. Yang, "A dynamic movement primitives-based tool use skill learning and transfer framework for robot manipulation," *IEEE Transactions on Automation Science and Engineering*, vol. 22, pp. 1748–1763, 2025.

[10] M. Tavassoli, S. Katyara, M. Pozzi, N. Deshpande, D. G. Caldwell, and D. Prattichizzo, "Learning skills from demonstrations: A trend from motion primitives to experience abstraction," *IEEE Transactions on Cognitive and Developmental Systems*, vol. 16, no. 1, pp. 57–74, 2024.

[11] M. H. Raibert and J. J. Craig, "Hybrid position/force control of manipulators," *Journal of Dynamic Systems, Measurement, and Control*, vol. 103, no. 2, pp. 126–133, 06 1981.

[12] S. Ruan, W. Liu, X. Wang, X. Meng, and G. S. Chirikjian, "Primp: Probabilistically-informed motion primitives for efficient affordance learning from demonstration," *IEEE Transactions on Robotics*, vol. 40, pp. 2868–2887, 2024.

[13] M. Arduengo, A. Colomé, J. Borràs, L. Sentis, and C. Torras, "Task-adaptive robot learning from demonstration with gaussian process models under replication," *IEEE Robotics and Automation Letters*, vol. 6, no. 2, pp. 966–973, 2021.

[14] L. Wang, G. Wang, S. Jia, A. Turner, and S. Ratchev, "Imitation learning for coordinated human–robot collaboration based on hidden state-space models," *Robotics and Computer-Integrated Manufacturing*, vol. 76, p. 102310, 2022.

[15] I. Rhee, G. Kang, S. J. Moon, Y. S. Choi, and H. R. Choi, "Hybrid impedance and admittance control of robot manipulator with unknown environment," *Intelligent Service Robotics*, vol. 16, pp. 19–60, 2023.

[16] T. Zhang, H. Sun, Y. Zou, and H. Chu, "An electromyography signals-based human-robot collaboration method for human skill learning and imitation," *Journal of Manufacturing Systems*, vol. 64, pp. 330–343, 2022.

[17] X. Yu, P. Liu, W. He, Y. Liu, Q. Chen, and L. Ding, "Human-robot variable impedance skills transfer learning based on dynamic movement primitives," *IEEE Robotics and Automation Letters*, vol. 7, no. 3, pp. 6463–6470, 2022.

[18] J. E. Colgate and G. G. Schenkel, "Passivity of a class of sampled-data systems: Application to haptic interfaces," *Journal of Robotic Systems*, vol. 14, no. 1, pp. 37–47, 1997.

[19] A. Q. Keemink, H. van der Kooij, and A. H. Stienen, "Admittance control for physical human–robot interaction," *The International Journal of Robotics Research*, vol. 37, no. 11, pp. 1421–1444, 2018.

[20] V. Duindam and S. Stramigioli, "Port-based asymptotic curve tracking for mechanical systems," *European Journal of Control*, vol. 10, no. 5, pp. 411–420, 2004.

[21] F. Ferraguti, N. Preda, A. Manurung, M. Bonfè, O. Lambercy, R. Gassert, R. Muradore, P. Fiorini, and C. Secchi, "An energy tank-based interactive control architecture for autonomous and teleoperated robotic surgery," *IEEE Transactions on Robotics*, vol. 31, no. 5, pp. 1073–1088, 2015.

[22] G. Raiola, C. A. Cardenas, T. S. Tadele, T. de Vries, and S. Stramigioli, "Development of a safety- and energy-aware impedance controller for collaborative robots," *IEEE Robotics and Automation Letters*, vol. 3, no. 2, pp. 1237–1244, 2018.

[23] C. Ott, A. Kugi, and Y. Nakamura, "Resolving the problem of non-integrability of nullspace velocities for compliance control of redundant manipulators by using semi-definite lyapunov functions," in *2008 IEEE international conference on robotics and automation*. IEEE, 2008, pp. 1999–2004.

[24] Y. Michel, C. Ott, and D. Lee, "Safety-aware hierarchical passivity-based variable compliance control for redundant manipulators," *IEEE Transactions on Robotics*, vol. 38, no. 6, pp. 3899–3916, 2022.

[25] Y. Yun, D. Oh, E. J. Song, H. R. Choi, H. Moon, and J. C. Koo, "Adaptive passivation of admittance controllers by bypassing power to null space on redundant manipulators," in *2024 IEEE/RSJ International Conference on Intelligent Robots and Systems (IROS)*, 2024, pp. 9292–9298.

[26] A. De Luca, A. Albu-Schaffer, S. Haddadin, and G. Hirzinger, "Collision detection and safe reaction with the dlr-iii lightweight manipulator arm," in *2006 IEEE/RSJ International Conference on Intelligent Robots and Systems*. IEEE, 2006, pp. 1623–1630.

[27] H. Khalil, *Nonlinear Systems*, ser. Pearson Education. Prentice Hall, 2002.